Channel interaction of the three $6pnd$ $J=3$ autoionizing series in barium

Oliver C. Mullins, Yifu Zhu, Emily Y. Xu, and T. F. Gallagher
Department of Physics, University of Virginia, Charlottesville, Virginia 22901
(Received 11 June 1985)

The energies and widths of a $6p_{3/2}nd$ $J=3$ autoionizing series are reported for $n=8$–17. Above the $6p_{1/2}$ ion limit the series is found to have approximately constant values for the quantum defect ($\mu \approx 2.85$) and for the scaled widths ($\Gamma_n n^{*3} \approx 0.07$ a.u.). Comparisons are made with the previously reported energies and widths of the other two $J=3$ $6pnd$ autoionizing series [F. Gounand *et al.*, Phys. Rev. A **27**, 1925 (1983)]. The interaction of all three series is analyzed using a six-channel multichannel-quantum-defect-theory model which successfully accounts for energies, widths, and complex excitation spectra for the three series. Conclusions concerning state wave functions are drawn from the data and implications regarding the strengths of different electron interactions are discussed. Additionally, information is obtained concerning the interaction of the bound perturber $5d\,7d\,{}^3F_2$ with the $6s\,14d\,{}^{1,3}D_2$ states.

I. INTRODUCTION

Autoionizing states of atoms present interesting examples of configuration interaction in two distinct ways. One consists of the interaction of discrete states with the continuum and the other consists of the interaction of two or more autoionizing series with each other. It is difficult to unravel the complexities associated with autoionizing states by the analysis of ground-state photoionization data because the resulting autoionizing series are often not well characterized in terms of the Rydberg electron and because of the often substantial direct photoionization process which results in Beutler-Fano profiles.[1] Furthermore, it is desirable to extend analyses of autoionizing series beyond limitations imposed by angular-momentum and parity selection rules applicable in ground-state photoionization. In addition, the theoretical analysis of experimental data on Rydberg and autoionizing series by the standard methods of configuration interaction is difficult and does not utilize Rydberg-series systematics at the outset.

Quite coincidently, new experimental and theoretical methods have been developed which allow for the production and analysis of autoionizing series. The experimental methods of the isolated core-excitation technique[2,3] result in relatively large cross sections for formation of well-defined autoionizing series. Additionally, there is virtually no continuum excitation, thereby preventing the complication of interferences between the discrete and continuum excitations. For data analysis the theoretical methods of multichannel quantum-defect theory (MQDT) allow one to treat interacting Rydberg series and their corresponding continua.[4–6] This theory describes the systematics and energy dependence of many atomic properties in terms of a few, relatively-energy-independent parameters. The combined application of the isolated core-excitation method with MQDT was first used to investigate autoionizing series of barium, namely three $J=1$ series[7] of the channel labels $6p_j ns_{1/2}$ and $6p_{1/2}nd_{3/2}$ and two $J=3$ series[8] with the channel labels $6p_{1/2}nd_{5/2}$ and $6p_{3/2}nd^+$ (our designation nd^+ will be explained later). More recently, features resulting from the second $6p_{3/2}nd$ series (hereafter designated $6p_{3/2}nd^-$) were observed as small shoulders (which are of somewhat lower energy than $6p_{3/2}nd^-$ states) on the dominant $6p_{3/2}nd^+$ peaks.[9] We, and simultaneously Van Woerkom and Cooke,[10] have found that when the bound $6snd\,{}^3D_2$ states are used as intermediate states (see Fig. 1) as opposed to the $6snd\,{}^1D_2$ states, then the $6p_{3/2}nd^-$ states are formed dominantly (with the appropriate photoexcitation) and therefore may be clearly observed.

Here, we report the positions and widths of the $6p_{3/2}nd^-$ states for $n=8$–17. Particular attention is given to understanding the excitation spectra of six $6p_{3/2}nd^{\pm}$ states which are below the $6p_{1/2}$ Ba^+ limit, i.e., for $n=8$–10. The spectra exhibit considerable structure, span a relatively large energy range, and correspond to low principal quantum number n, thereby providing stringent tests for our analysis. Previously, the

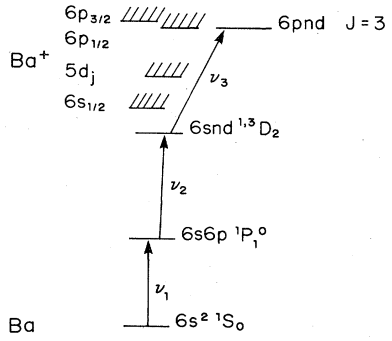

FIG. 1. Depicts the three-photon excitation scheme used to populate $J=3$ $6p_{3/2}nd$ autoionizing states, where laser number three performs the $6s_{1/2} \rightarrow 6p_{3/2}$ ion-core excitation. To form the $6p_{3/2}nd^-$ states dominantly, intermediate $^3D_2$ states are used, whereas to form the $6p_{3/2}nd^+$ states dominantly, intermediate $^1D_2$ states are used.

$6p_{3/2}10d^+$ spectrum was reported, as was its analysis,[8] which was based on the frame-transformation formulation of MQDT.[6] In addition, the analysis of the $6p_{3/2}10d^+$ spectrum has recently been described[11] using the MQDT formulation of the phase-shifted basis.[5,12,13] Using this phase-shifted formulation, we extend the analysis to include all three $J=3$ $6pnd$ autoionizing series by using a six-channel MQDT model (three bound and three continuum channels). Good accounting of all data, including the structured spectral densities, is obtained, and the extensive data can be represented in terms of a few parameters. Discrepancies between observations and predictions are noted and discussed. Properties concerning the continuum-state wave functions are obtained directly from the experimental data and implications concerning electron interactions are discussed. Finally, our data have a direct bearing on the interaction of the bound $6s\,14d\,^{1,3}D_2$ states with the $5d\,7d\,^3F_2$ perturber and corroborates recently reported results.[14]

In the sections that follow, we briefly describe our experimental approach, present our experimental results and the results of a MQDT analysis of the data, and finally discuss the implications of our observations.

II. EXPERIMENTAL APPROACH AND OBSERVATIONS

The experimental procedures used here are similar to those described elsewhere,[8] so only a brief summary is included here. As shown in Fig. 1 barium atoms are excited to the $6snd\,^{1,3}D_2$ states using two dye lasers, first exciting the $6s^2\,^1S_0$ ground-state atoms to the $6s\,6p\,^1P_1^0$ state and then exciting atoms from the $6s\,6p\,^1P_1^0$ state to the $6snd\,^{1,3}D_2$ states. Using a third dye laser we excite the $6p_jnd$ autoionizing states from the $6snd\,^{1,3}D_2$ states and detect the ions which result from the decay of autoionizing states. The three dye-laser pulses have typical parameters, 100 μJ energy, 5 ns duration, and 1 cm^{-1} linewidth.

An effusive beam of barium atoms is produced from a resistively heated oven and passes between two plates, one with a grid, where it is crossed by three collinear laser beams which perform the three sequential excitations (see Fig. 1). The laser beams are circularly polarized in the same sense so that only $J=3$ final states are formed. The ions are extracted through the grid and detected with a "venetian-blind" particle detector. The signal is collected by a boxcar averager and recorded on an X-Y plotter. As the $6snd\rightarrow 6pnd$ transition which is excited by the third laser is essentially the $6s\rightarrow 6p$ transition of the Ba^+ core with a spectator electron, it has an oscillator strength of one spread over the width of the $6pnd$ autoionizing state and is much stronger than the excitation to the underlying continuua. Thus, measuring the ion yield as the frequency of the third laser is scanned across the $6snd\rightarrow 6pnd$ transition directly reproduces the spectral density of the $6pnd$ state.[3] Usually, this leads to simple, nearly Lorentzian features whose center frequency and width give directly the energy and autoionization rate of the state in question. In the case of interacting autoionizing series more complex spectra are observed, reflecting the more complex structure of the autoionizing states themselves.

TABLE I. Frequency marker lines in the spectra.

A	B	C
$6s\,10d\,^1D_2$	$6s\,10d\,^3D_2$	$5d\,8s\,^1D_2$

In these experiments the relative frequency of the third laser was determined by monitoring its transmission through a 3.45-cm^{-1} free-spectral-range (FSR) étalon. The absolute frequency scale of the third laser is provided by sharp peaks which appear in the excitation spectra and correspond to the excitation from the $6s\,6p\,^1P_1^0$ state to higher bound states and their subsequent ionization, both transitions being pumped by the third laser. In Table I we label the lines which appear later in the figures.

As is often the case for a Rydberg state of a two-valence-electron atom, the total angular momentum j of the inner electron is a good quantum number. Indeed, the energy separation of $6p_{1/2}nd$ and $6p_{3/2}nd$ states is roughly 1700 cm^{-1}, which corresponds to the fine-structure splitting of the $6p$ state of the barium ion. Thus, one of the three $J=3$ $6pnd$ series is adequately described as $6p_{1/2}nd_{5/2}$[8] However, it is not obvious what angular-momentum quantum numbers should represent near constants of motion of the two $6p_{3/2}nd$ series. One of the two $6p_{3/2}nd$ series is formed dominantly when exciting $6snd\,^1D_2$ states and the other when exciting the $6snd\,^3D_2$ states. The $6snd\,^{1,3}D_2$ states are approximately singlets and triplets (based on energy splittings[15,16]) which project into jj coupling as $6s_{1/2}(\sqrt{2/5}nd_{3/2}+\sqrt{3/5}nd_{5/2})$ for the $^1D_2$ states and $6s_{1/2}(\sqrt{3/5}nd_{3/2}-\sqrt{2/5}nd_{5/2})$ for the $^3D_2$ states (the choice of the order of the angular-momentum coupling determines the phases). The observed intensities indicate that the two $6p_{3/2}nd$ series must project into jj coupling roughly as $6p_{3/2}(\sqrt{2/5}nd_{3/2}+\sqrt{3/5}nd_{5/2})$ for the higher-energy series designated as $6p_{3/2}nd^+$ and $6p_{3/2}(\sqrt{3/5}nd_{3/2}-\sqrt{2/5}nd_{5/2})$ for the lower-energy series designated as $6p_{3/2}nd^-$. As will be discussed, inclusion of small ($<20\%$) spin-orbit effects in the $6snd\,^{1,3}D_2$ states does not materially affect these conclusions.

By exciting the $6snd\,^3D_2$ states we have observed the $6p_{3/2}nd^-$ series, and in Table II the energies, quantum defects, and widths are listed for the $6p_{3/2}nd^-$ series for $8\leq n\leq 17$. Previously, the energies and widths of the $6p_{1/2}nd_{5/2}$ and $6p_{3/2}nd^+$ series were reported;[8] Fig. 2 shows the measured energy levels for states of the three $J=3$ $6pnd$ series. Above the $6p_{1/2}$ ion limit the $6p_{3/2}nd^-$ series has the approximate values for the quantum defects of 2.85 and for the scaled widths (Γn^{*3}) of 0.07 a.u. These values are to be compared with quantum defects of 2.74 and scaled widths of 0.11 a.u. reported by Gounand *et al.* for the $6p_{3/2}nd^+$ series.[8]

The previously reported[8] $6p_{3/2}14d^+$ state was misassigned and is, in fact, a member of the series reported here. The $6p_{3/2}14d^+$ state which we excited from the $5d\,7d\,^3F_2$ (which has substantial $6s\,14d\,^1D_2$ character) has energy 63 123.7 cm^{-1}, width 19 cm^{-1}, and quantum defect 2.73, which are in good agreement with the $6p_{3/2}nd^+$-series systematics. The excitation of both the $6s\,14d\,^1D_2$ and $6s\,14d\,^3D_2$ states results primarily in the

TABLE II. Energies, quantum defects, and widths for the $6p_{3/2}nd^-$ states. Experimental errors are shown in parentheses.

n	Energy (cm^{-1})	Quantum defect	Width (cm^{-1})
8	59 808(6)	2.876	85(6)
9	61 074(3)	2.863	52(4)
10	61 837.2(2)	2.856	a
11	62 332.7(1)	2.856	24(2)
12	62 679.5(1)	2.840	18.4(1)
13	62 922.0(1)	2.851	12.5(1)
14	63 103.9(1)	2.855	9.9(1)
15	63 243.3(1)	2.856	9.3(1)
16	63 353.2(1)	2.846	5.8(1)
17	63 440.6(1)	2.834	6.0(1)

[a]Channel interaction makes this value difficult to determine.

production of the $6p_{3/2}14d^-$ state. This is due to bound-state channel interaction and is described in Sec. IV.

Channel interaction assumes a particularly interesting form below the $6p_{1/2}$ ionization limit, where not only the interaction with the continuum occurs, but also the interseries interaction as well. Experimentally, by exciting the $6s_{1/2}\rightarrow 6p_j$ transitions of the ion core from the $6snd\ ^{1,3}D_2$ Rydberg states one can probe individually the $6p_jnd$ components of autoionizing-state wave functions.

Specifically, if the third laser wavelength is near the Ba^+ $6s_{1/2}\rightarrow 6p_{1/2}$ transition at 4935 Å, the $6p_{1/2}nd_{5/2}$ state or channel is excited. If the third laser wavelength is

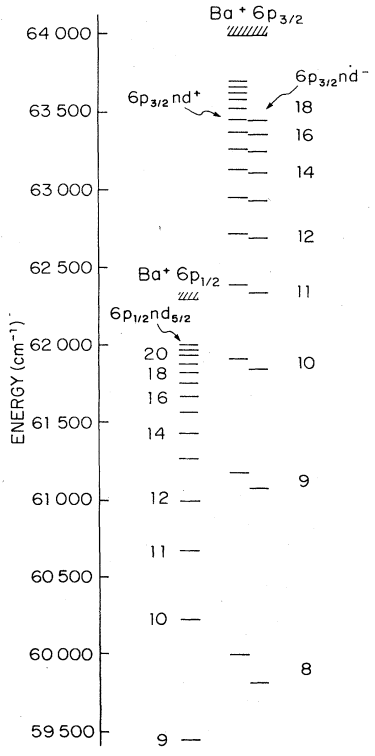

FIG. 2. Depicts the energy diagram drawn to scale for the $6p_{1/2}nd_{5/2}$, $6p_{3/2}nd^+$, and $6p_{3/2}nd^-$ autoionizing series. The energies for the first two series are taken from Ref. 8, and the energies for the $6p_{3/2}nd^-$ series are listed in Table II.

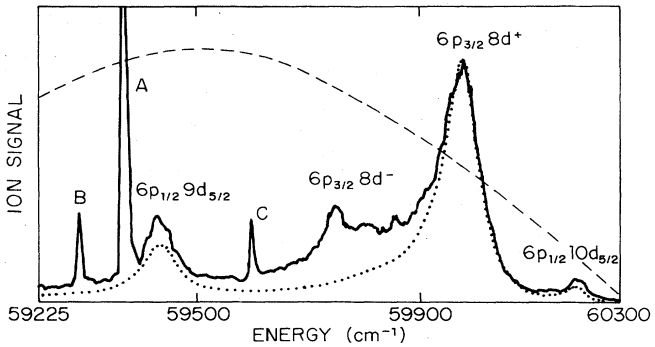

FIG. 3. This figure shows the $6s_{1/2}\rightarrow 6p_{3/2}$ excitation spectrum, which is obtained by exciting the $6s\,8d\ ^1D_2$ state and is dominated by the production of the $6p_{3/2}8d^+$ state. The solid line represents the data, while the dotted line represents the simulated spectrum based on our MQDT analysis. The appearance of the $6p_{3/2}8d^-$ and of some $6p_{1/2}nd_{5/2}$ states are labeled. The lines marked *A*, *B*, and *C* are spurious signals which serve as frequency markers. Their designations are listed in Table I and their source is described in Sec. II. The $6p_{1/2}10d_{5/2}$ peak is artificially small due to the laser gain curve, which is indicated by the dashed curve.

near the Ba^+ $6s_{1/2}\rightarrow 6p_{3/2}$ transition at 4555 Å, then two $6p_{3/2}nd$ series are excited in differing amounts where the excitation ratio is strongly dependent on the spin of the intermediate $6snd\ D_2$ state. Thus, we may obtain, separately, information about each of the three $6pnd$ $J=3$ channels.

Figures 3–8 depict the excitation spectra obtained by exciting the $6snd\rightarrow 6p_{3/2}nd$ transition from six bound states, the $6snd\ ^{1,3}D_2$ states for $8\leq n\leq 10$. Also shown in these figures are the simulated spectra which resulted from our MQDT analysis which will be described in the

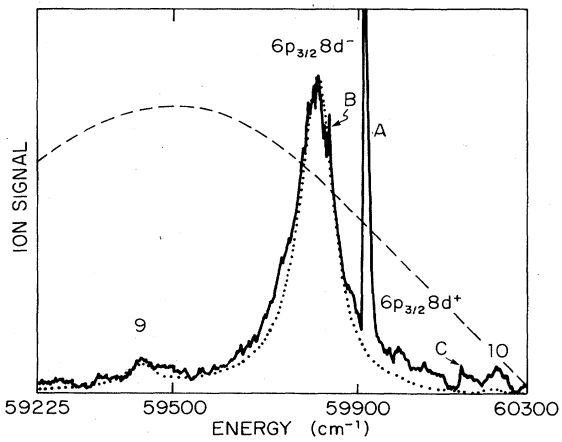

FIG. 4. This figure shows the $6s_{1/2}\rightarrow 6p_{3/2}$ excitation spectrum of the $6s\,8d\ ^3D_2$ state and is dominanted by the production of the $6p_{3/2}8d^-$ state. The solid line represents the data, while the dotted line represents the simulated spectrum based on our MQDT analysis. The appearance of the $6p_{3/2}8d^+$ state is indicated as are some $6p_{1/2}nd_{5/2}$ states (where only n is indicated). The peak labeled *A* is a frequency marker designated in Table I. The dashed line represents the dye gain curve.

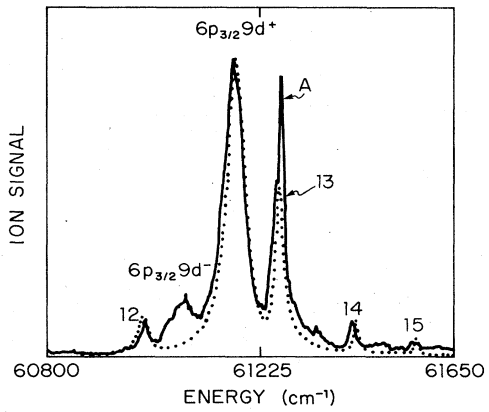

FIG. 5. This figure shows the $6s_{1/2}\rightarrow 6p_{3/2}$ excitation spectrum of the $6s\,9d\,{}^1D_2$ state and is dominated by the production of the $6p_{3/2}9d^+$ state. The solid line represents the data, while the dotted line represents the simulated spectrum based on our MQDT analysis. The appearance of the $6p_{3/2}9d^-$ state is indicated as are some $6p_{1/2}nd_{5/2}$ states (where only n is indicated).

following section. The $6p_{3/2}10d^+$ spectrum and its analysis were reported previously.[8]

In Figs. 3—8 we show the locations of the various $6p_{1/2}nd_{5/2}$ states (see Fig. 2) which produce the structure appearing in the spectra. As previously discussed,[7] the energies are not necessarily associated with peaks in Figs. 3—8, but can be associated with valleys in the spectra. Generally, channel interaction produces additional peaks (relative maxima) in spectra if the autoionizing states of different series are separated by more than their widths, and produces valleys (relative minima) if the states are separated by less than their widths.[7]

Collecting the excitation scans for the $6s\,10d\,{}^1D_2$ and particularly for the $6s\,10d\,{}^3D_2$ is difficult because the second laser which forms these states is efficient at photoionizing them. It is tuned near 4555 Å; these are marker lines *A* and *B* of Table I. Additionally, particularly for states of low principal quantum number n, the dye gain

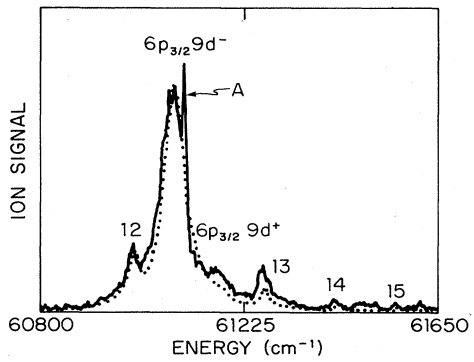

FIG. 6. This figure shows the $6s_{1/2}\rightarrow 6p_{3/2}$ excitation spectrum of the $6s\,9d\,{}^3D_2$ state and is dominated by the production of the $6p_{3/2}9d^-$ state. The solid line represents the data, while the dotted line represents the simulated spectrum based on our MQDT analysis. The appearance of the $6p_{3/2}9d^+$ state is indicated as are some $6p_{1/2}nd_{5/2}$ states (where only n is indicated).

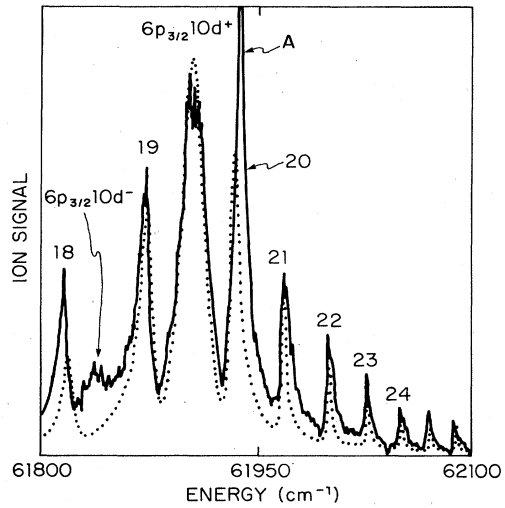

FIG. 7. This figure shows the $6s_{1/2}\rightarrow 6p_{3/2}$ excitation spectrum of the $6s\,10d\,{}^1D_2$ state and depicts the $6p_{3/2}10d^+$ state and its interaction with the $6p_{1/2}nd_{5/2}$ states. This spectrum and its analysis have been reported previously (Ref. 8). The solid line represents the data, while the dotted line represents the simulated spectrum based on our MQDT analysis. The $6p_{3/2}10d^-$ state is indicated as are some $6p_{1/2}nd_{5/2}$ states (where only n is indicated). As with all spectra reported here, the $6p_{1/2}nd_{5/2}$ states are not necessarily associated with the peaks, but can be associated with the valleys (Ref. 7).

curve varied appreciably over the width of the autoionizing resonances and was factored into the data analysis. We were unable to systematically study the $6p_j7d$ states due to their width in comparison to the dye gain curve.

III. MQDT METHOD

We employ the methods of MQDT to analyze our data. The application of MQDT to treat experimental data is described elsewhere,[5,6,12] so we discuss only a few basic principles here. Channel wave functions (ψ_i) for the atom are defined for $r\rightarrow\infty$ as consisting of a well-defined ion core and Rydberg function separable into radial and angular coordinates. The phase of the radial wave function is expressed as a superposition of the regular (f) and irregu-

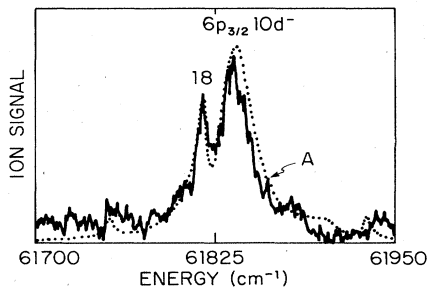

FIG. 8. This figure shows the $6s_{1/2}\rightarrow 6p_{3/2}$ excitation spectrum of the $6s\,10d\,{}^3D_2$ state and is dominated by the production of the $6p_{3/2}10d^-$ state. The solid line represents the data, while the dotted line represents the simulation based on our MQDT analysis. The appearance of the $6p_{1/2}18d_{5/2}$ state is indicated. Because the laser which excited the $6s\,10d\,{}^3D_2$ state was efficient in photoionizing this state, the noise level was increased.

lar (g) Coulomb functions,

$$\psi_i = \phi_i (c_i f - d_i g) \ . \tag{1}$$

ϕ_i represents the ion core and its angular-momentum coupling to the Rydberg electron. Channel interaction, which is inherent in an electron-ion collision, can be accounted for using the R matrix. By formulating the R-matrix equations of MQDT using an appropriately phase-shifted pair of Coulomb functions, MQDT parameters can be broken into two sets, the intrachannel parameters, the phase shifts given by the quantum defects, for idealized noninteracting channels, and the interchannel coupling parameters, the R'_{ij}, with vanishing diagonal elements.[5,12,13] We employ the formulation utilizing the phase-shifted basis as given by Cooke and Cromer, and the quantum defects and R-matrix elements reported here correspond to this phase-shifted formulation.[12] Additionally, this formulation allows for a number of parameters commensurate with the amount of experimental information. In particular, in our experiments no information is obtained corresponding to the absolute phases of the continuum channels and correspondingly, the theory does not contain information about these phases.

State wave functions are represented as superpositions of the channel functions,

$$\Psi = \sum_i Z_i \psi_i \ . \tag{2}$$

For closed channels the Coulomb functions consist of a divergent part which must have a vanishing coefficient, and this gives rise to the compatibility expression

$$| \tan(\pi \nu'_i) \delta_{ij} + R'_{ij} | = 0 \ . \tag{3}$$

For the autoionizing region state wave functions consist not only of bound parts but also of continuum parts. By appropriate choice of the continua one can represent n closed channels as interacting with n continuum channels which do not interact with each other without loss of generality (assuming, of course, that n continua exist). For n continuum channels there are n orthogonal (radial) wave functions at every energy which are superpositions of the bound and n continuum channels. The $r \to \infty$ boundary conditions for the radial wave function results in a set of homogeneous equations with a compatibility equation analogous to Eq. (3). Explicitly,

$$\begin{vmatrix} R'_{cc} + \tan(\pi \nu'_i) & R'_{co} \\ R'_{oc} & R'_{oo} + \tan(-\tau) \end{vmatrix} = 0 \ , \tag{4}$$

where the subscript c represents closed or bound channels, o open channels, and $\tan(\pi \nu_i)$ and $\tan(-\tau)$ are diagonal.[5,12] τ is the phase of the continuum channels for a particular state wave function. In solving for the spectral densities of autoionizing states, continuum normalization per unit energy is assumed.

To describe our data we have used a six-channel model which consists of three bound and three continuum channels. Thus, there are three orthogonal (radial) wave functions at any given energy which are comprised of a weighted sum of the six channel functions. The six $J=3$ channels are enumerated as

1	2	3
$6p_{1/2}nd_{5/2}$	$6p_{3/2}nd^+$	$6p_{3/2}nd^-$
4	5	6
continuum 1	continuum 2	continuum 3

where the $6p_{3/2}nd^+$ series is the higher energy of the two $6p_{3/2}nd$ series. The three continuum channels may be chosen to be orthogonal so that $R'_{45} = R'_{46} = R'_{56} = 0$. Channels 2 and 3, which converge to the same limit, are orthogonal by definition, so that $R'_{23} = 0$. To reduce the number of channel-interaction parameters, we constrain the model by requiring channel 1 to decay to continuum 1, channel 2 to continuum 2, and channel 3 to continuum 3. That is, we require

$$R'_{15} = R'_{16} = R'_{24} = R'_{26} = R'_{34} = R'_{35} = 0 \ .$$

Although this requirement is somewhat arbitrary we note that there is some justification. We performed a four-channel analysis with the same three bound channels and only one continuum channel; this model contained the same number of parameters as the six-channel model. The four-channel model was significantly inferior to the six-channel model, indicating that the bound channels do decay in appreciable measure to different continua. That orthogonal bound states decay in a large part to orthogonal continuum states is not entirely unexpected.

The values of the MQDT parameters resulting from our analysis are listed in Table III. The choice of the phases for the R-matrix elements relates to the excitation expression as will be described shortly. Previously reported parameters[8] which pertain only to channels 1 and 2 and their continua are in agreement with those listed in Table III. The widths of the autoionizing states are related to the (phase-shifted) R-matrix elements

$$\Gamma_j = \sum_o 2 R'^2_{jo} / \pi \nu^3 \ , \tag{5}$$

where o represents open channels. Above the $6p_{1/2}$ ionization limit, R'_{12} and R'_{13} contribute to the width of channels 2 and 3, respectively. Energy dependence was included for μ_3; this parameter was optimized for each of the three values of n used to produce the simulations in Figs. 3–8 and the corresponding values of μ_3 are listed in Table II. Energy dependence was included here due to the significant (but small) difference in quantum defects for different states of the $6p_{3/2}nd^-$ series. No energy dependence of the quantum defect for the low n states of the $6p_{3/2}nd^+$ series was found; the change in quantum defects being entirely accounted for by channel interaction

TABLE III. MQDT parameters obtained from our six-channel analysis of peak energies, widths, and excitation spectra.

$R'_{12} = 0.27$	$\mu_1 = 2.786$
$R'_{13} = 0.12$	$\mu_2 = 2.741$
$R'_{14} = 0.36$	$\mu_3 \sim 2.85$
$R'_{25} = 0.32$	
$R'_{36} = 0.31$	

described here. This illustrates that the energy dependence of MQDT parameters can be substantially different even for two similar autoionizing series of the same atom.

The excitation expression used to generate the simulations in Figs. 3—8 is now developed. Experimentally, the core excitation $6s_{1/2}\rightarrow 6p_{3/2}$ is performed; thus excitation into channels 2 and 3 can occur. The initial $6snd\ ^1D_2$ and $6snd\ ^3D_2$ states project into jj coupling, respectively, as

$$\begin{aligned}(^1D_2)&=6s_{1/2}(\alpha d_{3/2}+\beta d_{5/2})\ ,\\(^3D_2)&=6s_{1/2}(-\beta d_{3/2}+\alpha d_{5/2})\ .\end{aligned}\tag{6}$$

This projection allows some spin-orbit coupling to be introduced for these states which are dominated by their singlet and triplet character. Correspondingly, the $6p_{3/2}nd$ series are represented as

$$\begin{aligned}(6p_{3/2}nd^+)&=6p_{3/2}(ad_{3/2}+bd_{5/2})\ ,\\(6p_{3/2}nd^-)&=6p_{3/2}(-bd_{3/2}+ad_{5/2})\ .\end{aligned}\tag{7}$$

The transition amplitude for exciting $^1D_2$ and $^3D_2$ states can now be expressed in terms of the core excitation $6s_{1/2}\rightarrow 6p_{3/2}$ using standard angular-momentum algebra techniques.[17] The transition amplitudes T_i^S for exciting each spin state $S=0$ ($6snd\ ^1D_2$) and $S=1$ ($6snd\ ^3D_2$), respectively, to each of the final-state wave functions $\Psi_i(Z_2^i,Z_3^i)$ are

$$\begin{aligned}T_i^{S=0}&=[(a\alpha^{\frac{1}{2}}+b\beta^{\frac{1}{3}})Z_2^i+(b\alpha^{\frac{1}{2}}-a\beta^{\frac{1}{3}})Z_3^i]\\&\quad\times(6s_{1/2}||\mathbf{r}||6p_{3/2})\ \text{ for } ^1D_2\ ,\\T_i^{S=1}&=[(a\beta^{\frac{1}{2}}-b\alpha^{\frac{1}{3}})Z_2^i+(b\beta^{\frac{1}{2}}+a\alpha^{\frac{1}{3}})Z_3^i]\\&\quad\times(6s_{1/2}||\mathbf{r}||6p_{3/2})\ \text{ for } ^3D_2\ .\end{aligned}\tag{8}$$

Z_2^i and Z_3^i are the spectral amplitudes for channels 2 and 3, respectively, for the final-state wave function $\Psi_i(Z_2^i,Z_3^i)$ and are expressed parametrically in MQDT parameters by solving Eq. (4). The reduced matrix element is defined as in Ref. 17. Interference occurs between the excitation of channels 2 and 3 in the production of each eigenchannel Ψ_i (where Ψ_i is characterized by the continuum phase τ_i). As the final ion states Ψ_i are detected, no interference occurs between them and the total transition probability P^S for an intermediate state of spin S is

$$P^S=\sum_{i=1}^{3}|T_i^S|^2\ .\tag{9}$$

Phase information is retained only as products of radial functions dependent on Z_j^i and angular functions dependent on α, β, a, and b. The phases of the R-matrix elements reported here result when it is assumed that $\alpha,\beta,a,b>0$. The choice of this set of phases is described in Sec. IV.

Assuming the $6snd$ states to be predominantly singlets and triplets with 5% spin-orbit—coupling effects (giving $\alpha/\beta\approx 0.77$), we obtain from the analysis of excitation spectra (Figs. 3—8) the ratio of coefficients $a/b\approx 0.86$ for the excited stated $6p_{3/2}nd$ wave functions [see Eqs. (7)]. This ratio was not appreciably affected for assumed bound-state spin-orbit-coupling effects corresponding to $<20\%$ of the singlet-triplet splittings.

The six excitation scans of Figs. 3—8 provide a stringent test for our model because they are highly structured, span a large energy range, and correspond to states of low principal quantum number n. The simulations in these figures are fairly accurate in reproducing the experimental spectra with regard to peak (and valley) positions, widths, and relative cross sections. The conclusion is that our model and resulting MQDT parameters are reasonably accurate in describing the three $6pnd$ $J=3$ autoionizing series.

Some discrepancies between the data and simulations are apparent in Figs. 3—8. The small relative magnitude of the $6p_{3/2}nd^+$ peaks when exciting $^3D_2$ and of the $6p_{3/2}nd^-$ peaks when exciting $^1D_2$ could not accurately be reproduced by the simulations with one set of parameters. By making small adjustments in a/b for the continuum wave functions, good fits could be obtained for excitation scans either from the $6snd\ ^3D_2$ states or $6snd\ ^1D_2$ states for $n=9$ and 10, but not for both simultaneously. This suggests the existence of two ratios a/b for the wave functions, Eqs. (7), for $6p_{3/2}nd^{\pm}$ states, but we use the best-fit value to describe both $6p_{3/2}nd$ series due to an insufficient rationale for using two values of a/b. Additionally, for the $6p_{3/2}8d^+$ spectrum (Fig. 3) the occurrence of the $6p_{3/2}8d^-$ peak is at an unaccountably low energy. Both the difficulties of accounting for the relative ratios of peak positions[18] and peak heights have been found independently by Van Woerkom and Cooke[10] to exist above the $6p_{1/2}$ ionization limit, where they have carried out a more detailed study. The difficulties apparently do not result from the somewhat arbitrarily imposed constraints in our model of assigning certain R-matrix elements to zero.[10]

The quantum-defect surface for our six-channel model consists of a set of three surfaces defined by Eq. (4) in a cube with axis $\nu_{1/2}$, $\nu_{3/2}$, and τ_c, where τ_c is the continuum phase. The surface is triple-valued in the τ_c coordinate because there are three continua. Because this surface is difficult to represent in a useful way, we have instead constructed the Lu-Fano plot[19] for which the continua were ignored. Here we treat the problem as being a two-limit, three-*bound*-channel case. Figure 9 is the resulting approximate Lu-Fano plot constructed from the already determined quantum defects and the R-matrix elements R'_{12} and R'_{13}, where $R'_{23}=0$. Agreement between the data and calculated curve indicates that approximate values for the MQDT parameters can be obtained from Fig. 9 in spite of ignoring the continua. However, the continuum interactions cause several states to deviate from the calculated curve in Fig. 9. These deviations occur when state separations are smaller than state widths; the large widths are due to interaction with the continua. When states overlap channel interaction results in the appearance of structure (for example, see Fig. 7) and small energy shifts as opposed to large energy shifts [as predicted by Eq. (3)]. Thus, the direction and magnitude of the deviations for the states $6p_{1/2}nd$ for $n=18$ and 20—22 from the calculated, approximate curve in Fig.

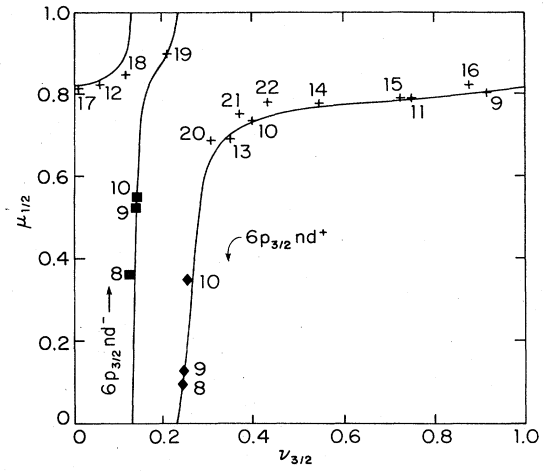

FIG. 9. This figure shows the Lu-Fano plot which results when continuum interactions are ignored. Because the state separations are generally greater than their widths, this plot is useful in predicting MQDT parameters. Deviations for the states $6p_{1/2}nd_{5/2}$, $n=18$ and 20—22, are largely due to continuum interactions as described in Sec. III.

9 result in large part from the continuum interactions. Nevertheless, the Lu-Fano plot is generally consistent with parameter values derived from the analysis of spectra, state energies, and widths. It should be noted that when the state separations are much smaller than the state widths, the approximate Lu-Fano plot where the continua are ignored can be very misleading for the estimation of MQDT parameters.[12]

IV. DISCUSSION

The angular-momentum description of the $6p_{3/2}nd$ series [$a/b \approx 0.86$ for Eqs. (7)] provides insight about electron interactions in the autoionizing-state wave functions. Various terms in the Hamiltonian can be examined to determine the source of splitting between the $6p_{3/2}nd^+$ and $6p_{3/2}nd^-$ series, and therefore the source of their angular-momentum descriptions. The quadrupole term of the Coulomb-interaction operator $1/r_{12}$ is the lowest-order direct term which contributes to splitting, and therefore is likely to be significant. It has recently been shown[20] that inclusion of only the direct quadrupole interaction can account for the splitting of the $6p_j ng_j$, states, which are therefore (j,k)-coupled. The radial integral of the quadrupole term F^2 is written as

$$F^2=\left[R_{6p_{3/2}}R_{nd'_j}\left|\frac{r_<^2}{r_>^3}\right|R_{6p_{3/2}}R_{nd_j}\right],$$

and is independent of j of the d electron to a very good approximation (only direct integrals are assumed). R_{nl_j} is the radial wave function of the electrons, and $r_<$ and $r_>$ correspond to operators for the smaller r and larger r electrons, respectively. The angular integrals of the quadrupole term can be expressed as

$$(j_p j'_d JM \mid C_1^2 C_2^2 \mid j_p j_d JM)$$

and can be evaluated by standard procedures.[17] Diagonalizing the quadrupole matrix one obtains the $|(jl)ksJ\rangle$ eigenfunctions in the jj basis; the higher-energy state $6p_{3/2}(\sqrt{32/35}nd_{3/2}+\sqrt{3/35}nd_{5/2})$ for $k=\frac{7}{2}$ and the lower-energy state $6p_{3/2}(\sqrt{3/35}nd_{3/2}-\sqrt{32/35}nd_{5/2})$ for $k=\frac{5}{2}$ (F^2 is assumed to be positive). We use these projections and the $6snd\ ^{1,3}D_3$ projections into jj coupling to assign $a,b,\alpha,\beta>0$ for Eqs. (6) and (7). The ratio of the coefficients, $a/b \approx 3.3$, is significantly different than that observed experimentally. The inescapable conclusion is that other terms of the Hamiltonian play a significant role in determining the splitting and state wave functions of the $6p_{3/2}nd^{\pm}$ series.

For the $6snd\ ^{1,3}D_2$ states the exchange energy dominates the spin-orbit coupling of the d electron. The exchange integral for these states enters through the quadrupole moment and is represented by G^2. For the $6p_{3/2}nd$ states the exchange integral enters through the dipole moment (G^1), and generally the F and G integrals are larger for lower order. The angular integrations for G^2 of the $6snd\ ^{1,3}D_2$ states and for G^1 of the $6p_{3/2}nd$ states result in similar factors. The splitting of the $6snd\ ^{1,3}D_2$ is roughly equal to the splitting of the $6p_{3/2}nd^{\pm}$ states (for the same n). Therefore, because exchange energy dominates the splitting of the $6snd\ ^{1,3}D_2$ states and because the exchange integral is of lower order for the $6p_{3/2}nd^{\pm}$ states which have comparable splitting to the $6snd\ ^{1,3}D_2$ states, it is reasonable to assume that the splitting of the $6p_{3/2}nd^{\pm}$ states is appreciably affected by exchange. The wave functions which we find experimentally can be obtained as eigenvectors of the electron-interaction Hamiltonian containing appreciable exchange dipole interaction and direct quadrupole interaction.

The bound-state perturbations of the $5d\,7d\ ^3F_2$ state and the $6s\,14d\ ^{1,3}D_2$ states produce an interesting effect in our observations. The $6s_{1/2}\rightarrow 6p_{3/2}$ excitation spectra of the $6s\,14d\ ^1D_2$ and $6s\,14d\ ^3D_2$ states are both dominated by the production of the $6p_{3/2}14d^-$ state, whereas the $5d\,7d\ ^3F_2$ state which is known to strongly interact with the $6s\,14d\ ^1D_2$ state results in the production of the $6p_{3/2}14d^+$ state. These observations are explained as follows. The zeroth-order positions of the $6s\,14d\ ^1D_2$ state and the $5d\,7d\ ^3F_2$ state are close in energy, with the doubly excited state being higher. Channel interaction causes these two states to repel, whereby the $5d\,7d\ ^3F_2$ state acquires appreciable $6s\,14d\ ^1D_2$ character. Thus, the $6s_{1/2}\rightarrow 6p_{3/2}$ excitation of the $5d\,7d\ ^3F_2$ state results in the production of the $6p_{3/2}14d^+$ state. The repulsion of the $5d\,7d\ ^3F_2$ and $6s\,14d\ ^1D_2$ states results in the $6s\,14d\ ^1D_2$ state becoming nearly degenerate with the $6s\,14d\ ^3D_2$ state. The $6s\,14d\ ^{1,3}D_2$ states repel each other and ultimately are separated by about 2 cm^{-1}. Again, state-wave-function mixing occurs, and because the $5d\,7d\ ^3F_2$ state has appreciable $6s\,14d\ ^1D_2$ character the Rydberg parts of both states labeled $6s\,14d\ ^1D_2$ and $6s\,14d\ ^3D_2$ have greater weighting of the $6s\,14d\ ^3D_2$ character. Thus, both states labeled $6s\,14d\ ^{1,3}D_2$ produce dominantly the (narrower) $6p_{3/2}14d^-$ peak in the $6s_{1/2}\rightarrow 6p_{3/2}$ excitation. A consequence of this picture is that the nominal $6s\,14d\ ^3D_2$ state possess $5d\,7d\ ^3F_2$ character and this has recently been shown.[14]

V. CONCLUSION

In this report we have treated in a unified manner extensive data, some which were obtained from a previous study[8] and some which were reported here for the first time. The data include the positions and widths of three $J=3$ autoionizing series—the $6p_{1/2}nd_{5/2}$, $6p_{3/2}nd^{+}$, and $6p_{3/2}nd^{-}$ series—and included highly structured excitation spectra for six states. These data can be represented with the methods of MQDT by a few physically meaningful parameters. Information about the state wave functions for the two $6p_{3/2}nd$ series is obtained directly from the data and implies that both the direct-quadrupole term and the exchange-dipole term of the $1/r_{12}$ operator are significant. In addition, conclusions concerning the nature of the interaction of the $5d\,7d\,^{3}F_2$ state with the $6s\,14d\,^{1,3}D_2$ states support recent findings.

ACKNOWLEDGMENTS

It is a pleasure to acknowledge the many fruitful discussions with Sten Salomonson. We are also very grateful to L. Van Woerkom and W. E. Cooke for providing us with unpublished data concerning the excitation of the $6p_{3/2}16d$ states from the $6s\,16d\,^{1,3}D_2$ states.

[1]U. Fano, Phys. Rev. **124**, 1866 (1961).
[2]W. E. Cooke, T. F. Gallagher, S. A. Edelstein, and R. M. Hill, Phys. Rev. Lett. **40**, 178 (1978).
[3]N. H. Tran, P. Pillet, R. Kachru, and T. F. Gallagher, Phys. Rev. A **29**, 2640 (1984).
[4]M. J. Seaton, Proc. Phys. Soc. London **88**, 801 (1966).
[5]M. J. Seaton, Rep. Prog. Phys. **46**, 167 (1983).
[6]U. Fano, Phys. Rev. A **2**, 353 (1970).
[7]W. E. Cooke and S. A. Bhatti, Phys. Rev. A **26**, 391 (1982).
[8]F. Gounand, T. F. Gallagher, W. Sandner, K. A. Safinya, and R. Kachru, Phys. Rev. A **27**, 1925 (1983).
[9]R. Kachru, H. B. van Linden van den Heuvell, and T. F. Gallagher, Phys. Rev. A **31**, 700 (1985).
[10]L. Van Woerkom and W. E. Cooke (unpublished).
[11]A. Giusti-Suzor and H. Lefebvre-Brion, Phys. Rev. A **30**, 3057 (1984).
[12]W. E. Cooke and C. L. Cromer (unpublished).
[13]A. Giusti-Suzor and U. Fano, J. Phys. B **17**, 215 (1984).
[14]O. C. Mullins, Y. Zhu, and T. F. Gallagher, Phys. Rev. A **32**, 243 (1985).
[15]M. Aymar and O. Robaux, J. Phys. B **12**, 531 (1979).
[16]P. Camus, M. Dieulin, and A. El Himdy, Phys. Rev. A **26**, 379 (1982).
[17]A. R. Edmonds, *Angular Momentum in Quantum Mechanics* (Princeton University Press, Princeton, N.J., 1960).
[18]Note the smaller quantum defects for the $6p_{3/2}nd^{-}$ states reported here than for the $6p_{3/2}nd^{-}$ features in the $6p_{3/2}nd^{+}$ spectra reported in Ref. 9.
[19]K. T. Lu and U. Fano, Phys. Rev. A **2**, 81 (1970).
[20]S. M. Jaffe, R. Kachru, H. B. van Linden van den Heuvell, and T. F. Gallagher, Phys. Rev. A **32**, 1480 (1985).